Compression of a confined semiflexible polymer under direct and oscillating fields

Keerthi Radhakrishnan[*] and Sunil P. Singh [†]

Department of Physics, Indian Institute of Science Education and Research, Bhopal 462 066, Madhya Pradesh, India

The folding transition of biopolymers from the coil to compact structures has attracted wide research interest in the past and is well studied in polymer physics. Recent seminal works on DNA in confined devices have shown that these long biopolymers tend to collapse under an external field, which is contrary to the previously reported stretching of the chain. In this work, we capture the compression of a confined semiflexible polymer under direct and oscillating fields using a coarse-grained computer simulation model in the presence of long-range hydrodynamics. In the case of a semiflexible polymer chain, the inhomogeneous hydrodynamic drag from the center to the periphery of the coil couples with the chain bending to cause a swirling movement of the chain segments, leading to structural intertwining and compaction. Contrarily, a flexible chain of the same length lacks such structural deformation and forms a well-established tadpole structure. While bending rigidity profoundly influences the chain's folding favorability, we also found that subject to the direct field, chains in stronger confinements exhibit substantial compaction, contrary to the one in moderate confinements or bulk where such compaction is absent. However, an alternating field within an optimum frequency can effectuate this compression even in moderate or no confinement. This field-induced collapse is a quintessential hydrodynamic phenomenon, resulting in intertwined knotted structures even for shorter chains, unlike other spontaneous knotting experiments where it happens exclusively for longer chains.

I. INTRODUCTION

Nanofluidic devices have been widely used for the characterization of macromolecules such as separation and sequencing of DNA [1–7], protein synthesis, transport of biopolymers, etc. [3–12]. The fluid flow in such narrow capillaries profoundly influences the structural [1,2,13–17] and dynamical behavior of soft-deformable macromolecules [1–7,18–23]. Few recent experiments have reported compression of a confined long DNA strand into isotropic globules under a uniform electric field [24–26], despite previously reported stretching of DNA seen under field [13,14,27–33]. Similar shrinkage of a confined polyelectrolyte chain has also been captured in simulations under an AC field [34], with the exception that the shrinkage was manifested as back-foldings rather than an isotropic compression. These works substantiate the inevitability of hydrodynamic interactions in inducing such compression. Similar, hydrodynamic flow-induced structural shrinkage is seen across diverse soft-matter systems such as the U-shape bending of elastic rods under field [35,36], shear-induced compaction [37,38], compaction of short chains under sedimenting fields [39,40], etc.

One direct repercussion of the chain compaction is the enhanced favorability of self-knotting observed within these structures. The formation of these spontaneous knots along a long polymer chain such as DNA [41–44] and other proteins [45,46] is a recurrent phenomenon in biological processes.

The use of chain compaction either by spatial confinement, compaction against slit barriers [47], or molecular crowding [48] has been deemed extremely useful in effectuating these knottings. The use of direct or oscillatory fields in dielectrophoresis is another important method for obtaining a spectrum of such self-entangled structures.

This article elucidates how a confined semiflexible chain exhibits large-scale compression under direct and oscillating uniform fields. The course of investigation is mostly steered along deciphering the sensitiveness of this intriguing phenomenon to varying physical complexities such as bending rigidity [49–51], degree of confinement [52–54], and chain length, along with a plausible driving mechanism which remains elusive so far. While the hydrodynamic flow field remains a precursor to such a phenomenon, the above factors also act as essential ancillaries in dictating the folding favorability.

The article is organized as follows: the simulation model and parameters are presented in Sec. II. All the results pertaining to chain conformation and dynamics under DC and AC fields are presented in Sec. III, which consists of four different sections. The summary of the results is discussed in Sec. IV.

II. MODEL

We model a semiflexible polymer along with solvent molecules confined in a cylindrical tube, periodic along its axis. The polymer is modeled as a bead-spring chain, which consists of N_m monomers. The bond connectivity between adjacent monomers is ensured using a harmonic potential $U_s = \sum_{i=1}^{N_m-1} \frac{k_s}{2}(r_{i,i+1} - l_0)^2$. Here, l_0 is the equilibrium bond

_____

[*]keerthirk@iiserb.ac.in

[†]spsingh@iiserb.ac.in

length, k_s is the spring constant, and $r_{i,i+1} = |\mathbf{r}_{i+1} - \mathbf{r}_i|$ denotes the magnitude of the ith bond vector. The semiflexibility is introduced via a bending potential, $U_b = \sum_{i=1}^{N_m-2} \frac{k_b}{2}(|\mathbf{r}_{i,i+1} - \mathbf{r}_{i+1,i+2}|)^2$, where $\mathbf{r}_{i+1,i+2}$ is the $(i+1)$th bond vector and k_b is the bending rigidity that dictates the stiffness. For the present model of semiflexibility, the bending rigidity k_b turns out to be approximately equal to the chain's equilibrium persistence length l_p in bulk. Here, l_p is the characteristic length scale at which the tangent-tangent correlations along a semiflexible chain in bulk decay off. Hence, throughout the work, this imposed bending rigidity will be variably referred to as k_b or persistence length l_p.

Furthermore, excluded volume interactions among the chain monomers are incorporated via the standard repulsive shifted Lennard-Jones (LJ) potential,

$$U_{LJ} = \sum_{i>j}^{N} 4\epsilon_{LJ}\left[\left(\frac{\sigma}{r_{i,j}}\right)^{12} - \left(\frac{\sigma}{r_{i,j}}\right)^{6} + \frac{1}{4}\right], \quad (1)$$

for $r_{i,j} \leqslant 2^{1/6}\sigma$ and $U_{LJ} = 0$, if $r_{i,j} > 2^{1/6}\sigma$. Here, σ is the bead diameter and ϵ_{LJ} is the LJ interaction energy.

The solvent molecules are modeled using multiparticle collision dynamics (MPC) [55,56], which is a particle-based mesoscopic simulation technique that incorporates both hydrodynamic interactions and thermal fluctuations. In this technique, solvent dynamics is updated via a streaming step, followed by a successive collision step [55,56] (at τ_s), where the exchange of momentum within fluid molecules happens, ensuring momentum conservation. The elaborate description of the method can be found in Refs. [15,55–59].

The interaction of monomers with the cylindrical channel is considered via a similar LJ potential described earlier in Eq. (1), where a monomer feels the repulsive force within a distance $R_c \leqslant 2^{1/6}\sigma/2$ from the channel wall. An external field G is imposed on all polymer monomers along the channel axis (here, in the x direction), while solvent molecules feel indirect drag via monomers. In the case of an oscillating field, a square-wave periodic force is applied to each monomer given as $F_G^x = \mathrm{sign}[\sin(2\pi\nu t)]G$. The force is directed along the channel axis, where ν (time period, $\tau_\nu = 1/\nu$) stands for the frequency.

The physical parameters are expressed in units of bond length l_0, energy k_BT, and time $\tau = \sqrt{m_s l_0^2/k_BT}$, where m_s is the mass of a solvent particle. The MPC parameters are collision time $\tau_s = 0.1\tau$, cell length $a = l_0$, and solvent density $\rho_s = 10m_s/l_0^3$. The spring constant is $k_s = 10000(k_BT/l_0^2)$, LJ energy is $\epsilon_{LJ}/k_BT = 1$, and the mass of the monomers is chosen as $M = 10m_s$. The bending rigidity of the chain is varied in the range of $k_b = 0$–25. This corresponds to the equilibrium persistence length of a semiflexible chain in bulk, $k_b \approx l_p$ (both in dimensionless units, for the model chosen in our case). Newton's equations of motion of the polymer are numerically solved using the velocity-Verlet algorithm at fixed integration time step $h_m = 5 \times 10^{-3}\tau$. If not mentioned otherwise, all results are for the chain length $N_m = 200$. We use a certain mapping to obtain the experimental scales, equivalent to our coarse-grained model. This protocol has been previously found to be efficient in explaining many DNA-based phenomena [60,61]. A double-strand DNA
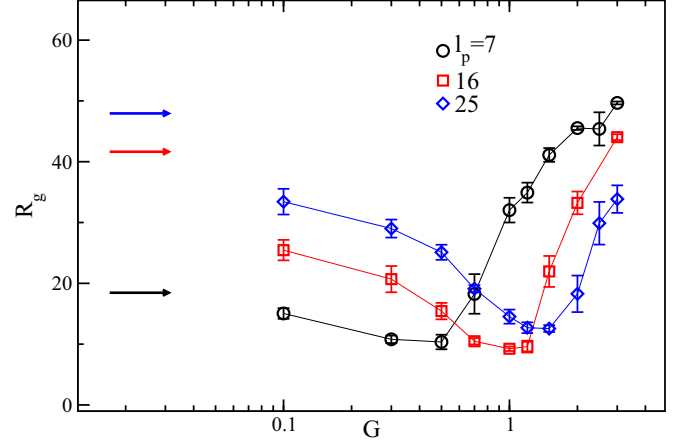
FIG. 1. Radius of gyration, R_g, of a semiflexible polymer under a DC field (G) for various persistence lengths l_p in pore radius $R_p = 10$.

of width $w \approx 2$ nm, $l_p \approx 50$ nm, and contour $L = 16\,\mu$m is equivalent to a chain of bead diameter $\sigma = 0.8$, $l_p = 20$, and $N = 6400$. Considering each base pair to be of mass 615 Da, a monomeric unit of length 2 nm (12 bps) has a mass of 7380 Da, which is equal to $M = 10$, a monomer's mass in simulations units. Hence, our simulation time unit $t = \sqrt{m_s l_0^2/K_BT} = 1$ translates as $t = 4.3 \times 10^{-6}$ sec in real units. So, the chosen window of frequencies 0.0001–0.02 can be mapped to 23–4600 Hz for a chain length equivalent to $N_m = 200$.

III. RESULTS

We present the structural response of a confined semiflexible chain under a uniform field. For that, we follow a systemic approach of addressing the influence of direct fields, followed by an investigation into oscillatory fields.

A. Chain collapse under direct field

In bulk, it is preestablished that a short flexible chain exhibits weak compression under a direct field [33,37]. Figure 1 elucidates the structural response of a confined semiflexible polymer ($N_m = 200$) under subjection to a constant DC field. This is parametrized in terms of the average radius of gyration, given as $R_g = \sqrt{\langle\frac{1}{N_m}\sum_{i=1}^{N_m}(\mathbf{r}_i - \mathbf{R}_{cm})^2\rangle}$, where $\mathbf{R}_{cm}$ is the center of mass of the chain. The retrieved curve exhibits a nonmonotonic dependence over G, where, within a moderate field strength, the chain exhibits a significant structural compression, followed by stretching at higher field strengths [37]. This is qualitatively similar to the stretching response reported for the flexible chain in bulk, with the exception that their chain compaction was seen only for smaller chain lengths and weak field [39,40]. However, for a confined semiflexible chain, not only the reduction become prominent for $N_m = 200$, but the favorability of the induced compression shifts toward higher fields with increasing persistence length. Also, the relative compaction gets more pronounced for higher bending rigidities; for example, for $l_p = 25$ it is roughly $R_g/R_g^0 = 0.25$,

while for $l_p = 7$, $R_g/R_g^0 = 0.5$, with R_g^0 being the radius of gyration of the chain in equilibrium. This is particularly fascinating considering the long and semiflexible nature of a typical DNA molecule [62] which reportedly exhibits collapse under applied fields [24–26].

Effect of bending rigidity. In the equilibrium, it is preestablished that a confined chain exhibits a monotonic stretching with increasing persistence length, where the chain with lower bending rigidity spanning the de Gennes regime and moderately confined de Gennes regime [63–65] ($D/l_p \gg 1$) takes a coil-like structure. However, with enhancing chain rigidity, it transitions into Odijk's regime [16,66] ($D/l_p < 1$), exhibiting stretching into a linearly arranged array of the chain segments. The equilibrium curve is shown in Fig. 2(a). However, the chain exhibits a counterintuitive structural response with bending rigidity under a direct field, shown in Fig. 2(b). The R_g is normalized with the stretching of a flexible chain, R_g^{flx}. A flexible chain ($l_p = 0$) takes up a tadpolelike structure [39,40] made of a compact head followed by an extended tail, as shown in Fig. 2(c). However, with increasing bending rigidity (l_p), the chain takes up a folded structure with a short fluctuating tail. This manifests as the compression seen in the intermediate l_p regime, elucidated for $l_p = 13$ in Fig. 2(c). Further, beyond a certain l_p, the chain stretches again [see $l_p = 30$ in Fig. 2(c)].

A similar phenomenon has been previously reported in the case of elastic filaments that undergo a counterintuitive bent deformation under a sedimenting field [35,36]. These works attribute the coupling of long-range hydrodynamic force fields with the chain contour. In the presence of the external force, the chain experiences enhanced drift in the center due to the addition of velocity fields from both ends, compared to the lagging terminal ends. As a result of this inhomogeneity in the hydrodynamic drag experienced by the chain across its contour, the chain attains a bent U shape with a uniform drift. This insight might suffice to qualitatively explain why a long semiflexible chain tends to fold and crumble instead of stretching under an external field. While in the case of a flexible chain, it is preestablished that the chain stretches into a tadpole state [39,40] such that the small bundling in the head region experiences similar friction as that of the lagging tail end [see Fig. 2(c), $l_p = 0$]. This eventually results in a uniform drift. However, a chain with a finite amount of bending, such as an elastic filament, might undergo some bent deformations under inhomogeneous flow. Following this, we estimate the flow profile of the chain under the field using a quiver plot, shown in Fig. 3. The arrow indicates the mean velocity V_i of the chain segment with respect to the chain's center of mass, where the position of the arrow represents the respective chain segment's distance from the chain's center of mass. Hence, V_i is given as $V_i = \frac{d(\mathbf{r}_i - \mathbf{r}_{cm})}{dt}$, where $\mathbf{r}_i$ and $\mathbf{r}_{cm}$ are the positions of the ith segment and the chain's center of mass, respectively.

The flow profile of chains with bending rigidities $l_p = 13$ and $l_p = 20$ where structural folding happens are shown in Fig. 3. A circulatory flow with vortices on both sides of the axis of the chain is obtained. For $l_p = 13$, x is the direction of the chain's drift or the field direction; then segments close to the chain's center $y \to 0$ drift in the field direction, contrary to the one at the periphery $y \sim \pm 4$ that lags and is pulled
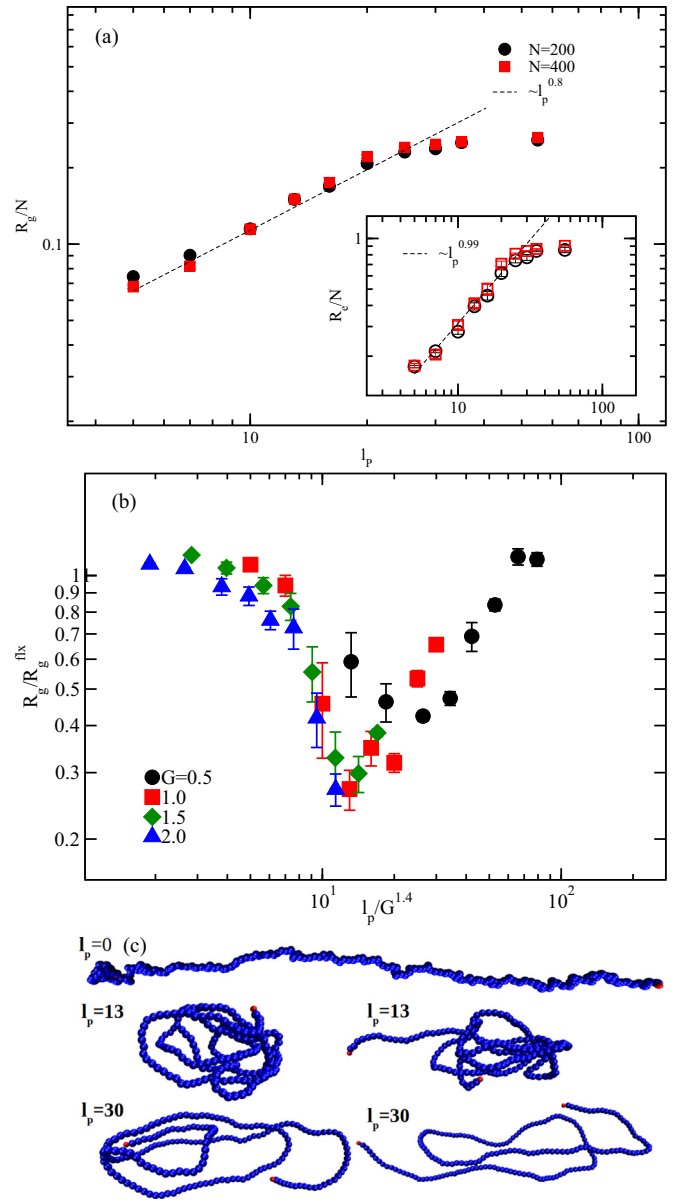
FIG. 2. (a) Scaled radius of gyration, R_g, of a semiflexible polymer chain with varying persistence length l_p in confinement radius $R_p = 10$ for two different chain lengths. Inset: The variation in end-to-end distance R_e. (b) The R_g of a confined chain in pore ($R_p = 10$) as a function of l_p for a fixed G. The chain undergoes a collapse in DC beyond a critical l_p. (c) Snapshots of the chain under DC for various l_p at $G = 1$ and $N_m = 200$. All the plots and conformations of the chain correspond to the DC field.

back. This is because, under subjection to an external field, the monomers in the periphery experience an enhanced hydrodynamic drag compared to those inside the coil [39,40]. As a result of this spatial heterogeneity in the drag force, the segments in the center of the coil drift faster compared to the peripheral ones, and the same when looked at from the chain's center-of-mass frame will give a recirculatory profile where the lagged particles from the surface flow back into the middle. In a semiflexible chain with finite bending, any force can propagate smoothly along the chain segments such that the
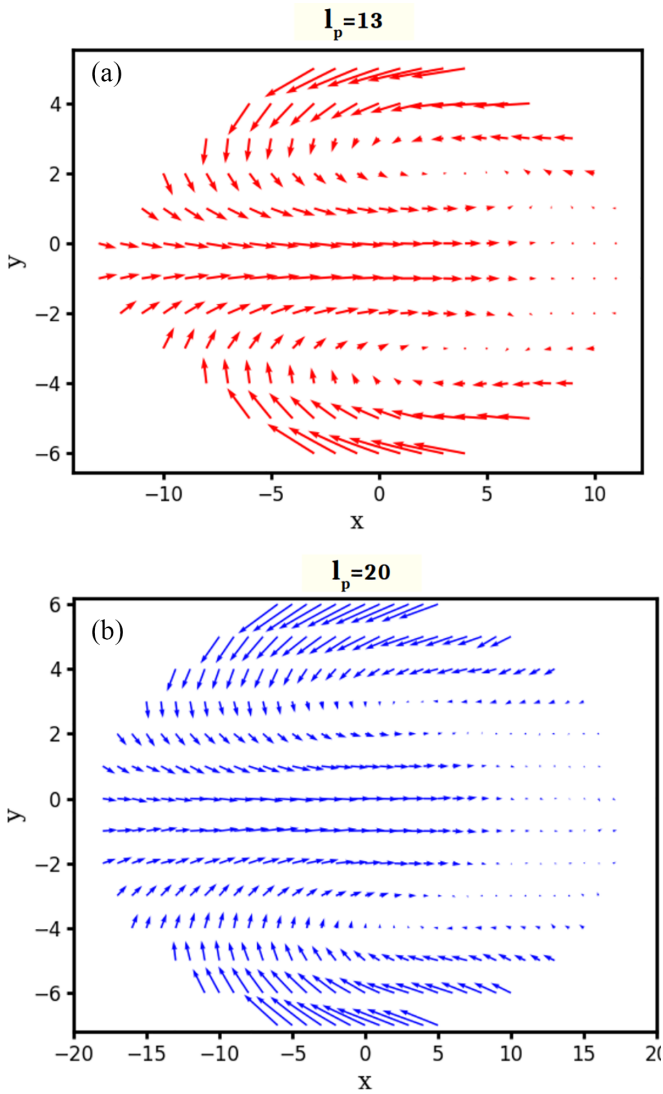
FIG. 3. Velocity profile of monomers with respect to the center of mass of the chain under subjection to a direct field for (a) $l_p = 13$ and (b) $l_p = 20$, where the polymer undergoes structural compaction. The chain undergoes a recirculatory motion, where, towards the center, the chain segments drift faster, while the outermost part gets lagged and constantly pushed back towards the center in a swirling motion, eventually leading to chain intertwining and compaction. The pore is fixed at $R_p = 10$ and the DC field strength $G = 1.0$.

force gradient from the center to the periphery couples with the chain rigidity to generate torque and induce chain folding. However, due to the ineffectiveness of a force-induced torque, a structurally folded state is not observed in the case of a completely flexible chain [39,40]. While at intermediate l_p, the hydrodynamic flow instigates substantial structural folding, at larger l_p's, the increase in bending stiffness disfavors large curvatures, resulting in elongated backfolded domains instead of compact structures [see $l_p = 30$ in Fig. 2(c)]. In summary, the nonmonotonic response of the chain under the DC field can be seen as a competition between the hydrodynamic drag-induced folding [39,40] and the bending energy cost.

A similar nonmonotonicity is also observed in the case of spontaneous knot formations of the polymers [51,67]. This
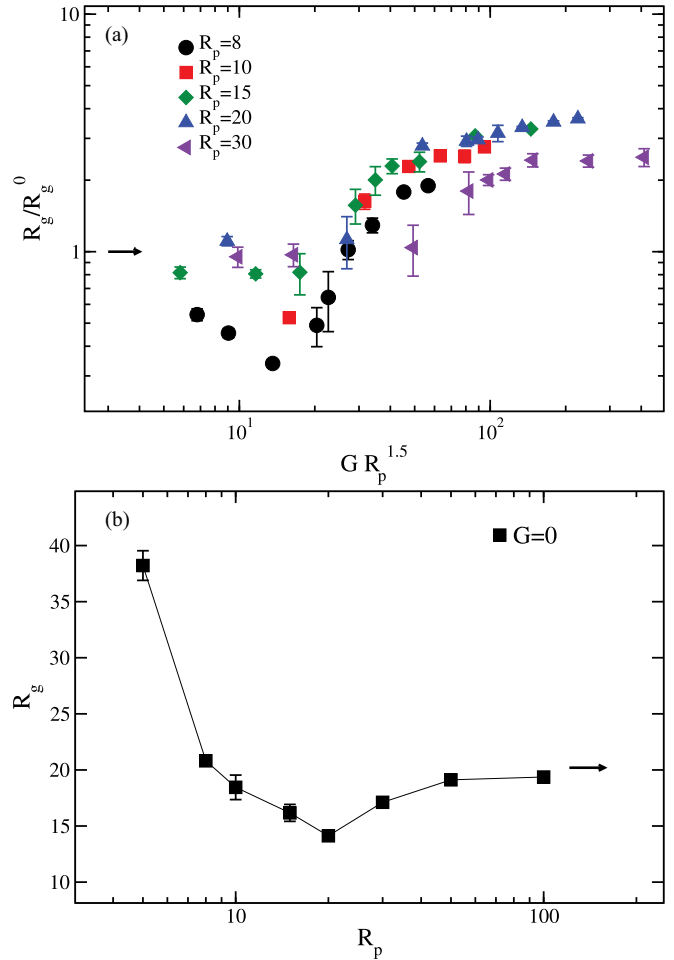
FIG. 4. (a) The normalized radius of gyration of a chain at $l_p = 7$, as a function of G for a range of confinements under a DC field. Note that the x axis is scaled with $R_p^{1.5}$. (b) The equilibrium radius of gyration of a confined semiflexible chain as a function of pore radius at $l_p = 7$ for chain length $N_m = 200$.

similarity can be drawn considering the self-entangled and knotted structures found in our case, which will be corroborated later in the manuscript. A heuristic scaling obtained for the critical bending rigidity beyond which the chain starts compressing indicates $l_p^c \sim G^\beta$ kind of dependence, where exponent is $\beta \approx 1.4$.

Effect of confinement. Considering how confinement affects the conformational dynamics of a chain [16,64,65], it is indispensable to look at the influence of the geometric constraint. Figure 4(a) elucidates the field-induced compression of a semiflexible polymer ($l_p = 7$) for a range of varying pore radii. The obtained results suggest that a polymer under strong confinement ($D/2l_p < 1.4$) undergoes a substantial compression at lower field strengths, followed by stretching. However, a chain under moderate or weak confinement ($D/2l_p > 1.4$) exhibits no compression and undergoes a monotonic stretching. This is evident in $R_p \leqslant 10$, where a compressive dip in R_g is seen for lower G values, while for $R_p > 10$, only monotonic stretching is seen, devoid of any shrinkage. In other words, a minimum bending rigidity is required to reinforce the folding as elucidated in the previous section; however,

this bending threshold can go to lower values of l_p for a higher degree of confinement. For pore $R_p = 8$, the feasible range for effectuating chain folding includes $l_p = 7$; however, for other pores, the bending threshold is possibly higher and hence no folding is seen at $l_p = 7$. At stronger confinements, when the pore diameter is comparable or less than $2.8l_p$, the wall constriction substantially enhances the effective bending cost more than the one stemming from the intrinsic bending. With this confinement-enhanced bending rigidity, the chain segments might tend to strongly couple to the field-induced inhomogeneous drag, giving rise to recirculatory structures. Even studies on knots in confined polymers report a behaviorally similar trend where narrower confinement shifts the minima of the free energy cost of knotting to lower bending rigidities [68].

Also, a heuristic scaling obtained in Fig. 4(a) for the field beyond G_c in which stretching is effectuated gives a $G_c \sim R_p^{-1.5}$ dependence. The deviation in the scaling of R_p seen for the case of $R_p = 30$ is the repercussion of R_p hitting a different regime, where the effect of confinement diminishes such that, for all pores with $R_p > 20$, it tends to the bulk behavior. This is elucidated in Fig. 4(b), which shows the structural variation of a chain under varying confinement in equilibrium. It shows a typical nonmonotonous pattern, as reported earlier [69], where the chain swells back to its bulk value beyond $R_p > 20$.

B. Chain under oscillating field

The structural response of the chain under an oscillating field is shown in Fig. 5(a) for $l_p = 7$ and $R_p = 10$. Here chain remains essentially unperturbed at higher frequencies, retaining the equilibrium structure (R_g^0). In the intermediate frequencies, the chain swells along the field direction, referred to as the *stretch state*, until it reaches a critical frequency ν_c, below ν_c chain undergoes a significant collapse. The *compressed state* essentially consists of a folded structure with a short fluctuating tail. This collapse is further followed by stretching at lower frequencies approaching the DC-like behavior. Unlike the stretch state mentioned earlier, the chain structure is more like a *tadpole* with a leading bob-head and trailing long tail that switch the direction at every field switch. This eventually merges with the DC limit, where, for long chains, a tadpole structure is observed with a long trailing end [37,39,40]. In summary, for a range of $\nu \ll \nu_c$, $\nu < \nu_c$, and $\nu \gtrsim \nu_c$, the chain undergoes a three-state transition involving *tadpole-collapse-stretch* states, respectively (see the Supplemental Material, Movie 1 [70]).

A scaling of R_g with ν/G is procured, where all the curves superimpose on each other, suggesting a linear dependence of ν_c with G. The striking observation here is that for $l_p = 7$, the chain stretches under the DC field for $G > 1$ (see Fig. 1). However, the oscillating field drives the system to a compressed state for the same field strengths. Similar AC-induced compressions are seen for other bending rigidities, $l_p = 16$ and $l_p = 25$ (see the Supplemental Material, Movie 2 [70]), shown in Figs. 5(b) and 5(c) for a wide range of G beyond the linear response regime, which is devoid of chain foldings in DC. Another impressive feature of the AC-driven compression is that the same extent of the collapse is attainable
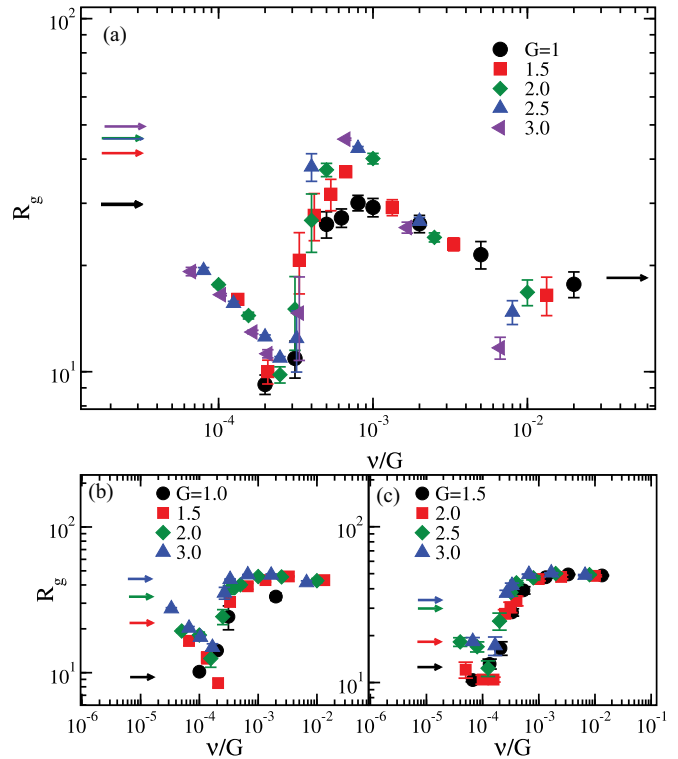
FIG. 5. The variation of R_g in response to varying field frequencies (AC field) for different G and fixed $R_p = 10$. Different panels correspond to persistence length: (a) $l_p = 7$, (b) $l_p = 16$, and (c) $l_p = 25$. The R_g for the respective DC values are denoted by a horizontal arrow.

across all these field strengths, while the maximum collapse possible varies, $R_g/R_g^0 = 0.55, 0.25, 0.2$, for persistence lengths $l_p = 10, 16$, and 25, respectively. Further, the transition points for the collapse obtained in Figs. 5(a)–5(c) indicate that the retrieved critical frequency ν_c/G is nearly independent of the persistence length of the chain.

Effect of confinement under AC field. The effect of confinement on the structural response of a chain for different pore radii is displayed in Fig. 6(a), at $l_p = 7$ and $G = 2.0$. For a narrow pore $R_p \lesssim 10$, with decreasing frequency, a three-tier stretch-collapse-tadpole kind of transition is observed, while with increasing pore radii, the stretching before collapse (for $\nu \gtrsim \nu_c$) diminishes, as is evident in the case of $R_p = 15, 20$, and 30, which is devoid of such stretching.

Additionally, a nonmonotonic shift in the critical frequency ν_c with pore radius is seen, where, beyond $R_p = 20$, the ν_c decreases. This may be stemming from similar nonmonotonicity seen in equilibrium R_g, as shown in Fig. 4(b). Further, the structural response of the chain obtained for $R_p = 20$ and $R_p = 30$ for varying fields is shown in Figs. 6(b) and 6(c). This exhibits a strong coil to compressed-state transition at the critical frequency before tending to the DC limit. See the Supplemental Material, Movie 2, for the conformations of compressed states for different pore radii [70]. Here, we retrieve a scaling for the critical frequency with field strength as $\nu_c \sim G$ for $R_p = 20$, similar to the case of $R_p = 10$, while for $R_p = 30$, we get $\nu_c \sim G^{0.6 \pm 0.02}$. This difference is speculated to be a result of the chain hitting the bulk regime beyond
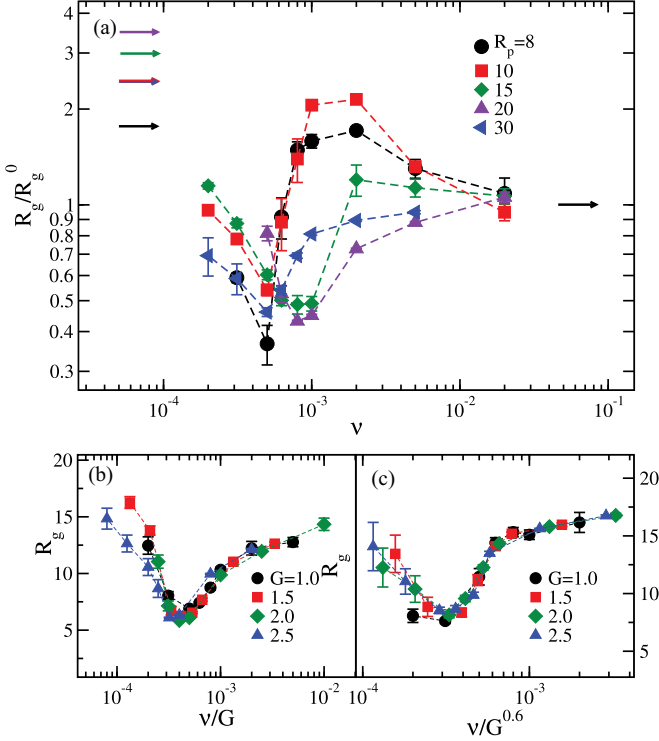
FIG. 6. (a) Scaled radius of gyration, R_g/R_g^0, of a semiflexible chain in response to varying field frequencies (AC field) at $G = 2$, for different pore radius R_p. Horizontal lines denote values of R_g/R_g^0 for the DC field. Here, (b) and (c) correspond to the variation in R_g of the polymer chain under confinement in response to changing frequencies for a given AC field strengths G, for pore radii $R_p = 20$ and 30, respectively.

FIG. 7. Longitudinal and transverse components of the radius of gyrations, G_{xx} (square) and $G_{yy} + G_{zz}$ (diamonds), along with the radius of gyration (bullet) for a few pore radii, including bulk under the AC field. The values correspond to $N_m = 200$ and $l_p = 7$ for all pores, while the bulk is shown for $N_m = 50$, $l_p = 7$. The stretching at a lower pore radius ($R_p = 10$) is effectuated by pore-enhanced elongation along the field axis. The stretching in bulk is attributed to the stretching and alignment of the chain along the transverse directions.

$R_p = 20$; see Fig. 4(b). Previously, we have seen that in DC for narrow pores, strong compression at lower fields is seen in contrast to wider pores (like $R_p = 20$ and 30), where no such folding happens [see Fig. 4(a)]. Interestingly, under an oscillating field, not only narrow pores [$R_p = 10$ in Fig. 5(a)], but even larger pores [$R_p = 20$ and 30 in Figs. 6(b) and 6(c)] exhibit remarkable compression of the chain for a range of field strengths, where the chain remains stretched under the DC field. Hence, an AC-driven collapse mechanism is accessible over a wider range of confining radii (including bulk) and field strengths beyond the linear response regime.

To gain insights into the various stretching responses seen for different pores in Fig. 6(a), we distinctly look into the chain's expanse in the longitudinal and transverse directions to the applied field. Figure 7 shows the radius of gyration, $R_g^2 = \langle \frac{1}{2N^2} \sum_{i,j} (\mathbf{r}_i - \mathbf{r}_j)^2 \rangle$ (in black circles), its component along the x direction of the confinement axis, $G_{xx} = \langle \frac{1}{2N^2} \sum_{i,j} (x_i - x_j)^2 \rangle$ (in red squares), and its component in the perpendicular $y - z$ plane, $G_{yy} + G_{zz} = \langle \frac{1}{2N^2} [\sum_{i,j} (y_i - y_j)^2 + \sum_{i,j} (z_i - z_j)^2] \rangle$ (in blue diamonds), for varying pore radii $R_p = 10$, 15, 30, and bulk depicted in a clockwise manner from the top left, respectively. Interestingly, for $R_p = 10$, the G_{xx} curve maps the overall R_g^2, suggesting that the stretching observed here is by virtue of the chain extension along the channel axis. The transverse component that is barely contributing gives a highly anisotropic stretched

state. However, with increasing pore radii, such as for $R_p = 15$, the x component departs away from the overall R_g, and the contribution from the transverse component enhances, decreasing the anisotropy along the field direction. Interestingly, with further increase in the pore radius such as for $R_p = 30$, the structure again shows an increasing anisotropy by preferentially aligning in the $y - z$ plane. Further, tending to the bulk case, the chain again exhibits prominent transverse alignment for higher frequencies, where $(G_{yy} + G_{zz})/G_{xx} > 2$. Hence, it can be inferred that at higher frequencies where the field switch happens relatively faster, a chain in bulk or in weak confinement ($D \gg l_p$) tends to preferably reorient in the transverse direction in response to the field, instead of stretching along the axis. However, beyond a certain critical confinement, when D becomes comparable to the scales of l_p and the presence of a wall becomes prominent, this transverse alignment of the chain is constricted by the wall, resulting in an effective stretching along the channel axis.

Effect of bending rigidity under AC field. Now, we consider the explicit effect of bending rigidity on the chain's collapse mechanism under the AC field. This is shown in Fig. 8 for different bending rigidities at $G = 2$ and pore radius $R_p = 10$ (diameter $D = 20$). More flexible chains undergo a *stretch-collapse-tadpole* state transition while going from higher to lower frequency in the respective window of $\nu \geqslant \nu_c$, $\nu < \nu_c$, and $\nu \ll \nu_c$. The stretching observed at higher frequencies prior to the compression is suppressed with increasing bending stiffness. For example, beyond $l_p > 13$, stretching is completely absent and the chain undergoes a direct collapse transition. Similar to the previous case of $R_p = 10$ displayed in Fig. 7, here also at moderately strong confinements where D is comparable to the scales of l_p (yet $D \geqslant 2l_p^c$), the geometric constriction restricts any transverse alignment and leads to chain stretching along the channel axis under an applied field. However, with further increase in persistence length,
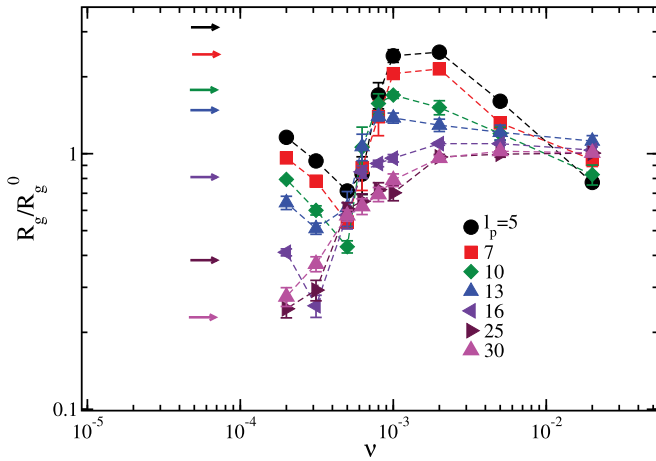
FIG. 8. The normalized radius of gyration, R_g/R_g^0, of the chain at $R_p = 10$ in response to varying frequency at $G = 2$, for different persistence length l_p under an AC field. The horizontal arrows denote the DC values of R_g/R_g^0 ($\nu = 0$).

FIG. 9. Scaled radius of gyration, R_g, of the polymer chain in pore $R_p = 10$ in response to varying field frequencies at $G = 2$, for different chain lengths (N_m) under a DC field. Horizontal lines denote the R_g values for the same DC field.

especially when $D < 2l_p^c$, the effect of confinement grows immensely stronger such that even in equilibrium ($G = 0$), the chain stretches into a linearly arranged array of chain segments [16,66] along the channel axis [as in Fig. 2(a)]. In this case, further subjection to an external field might bring only a nominal difference to an already stretched stiff confined chain. This is why, in the case of chains with larger persistence lengths compared to the pore diameter (i.e., $l_p > 13$ where $2l_p^c > D$), the R_g seems almost unaltered from its equilibrium value R_g^0 at higher frequencies.

In summary, for a confining radius, there exists a critical persistence length $D/2l_p^c \approx 1.0$ beyond which the chain eludes the prestretching tendency before collapsing at high frequencies ($\nu > \nu_c$). Also, for higher persistence lengths, the folding favorability enhances dramatically and the chain exhibits collapse for a wide range of frequencies, even extending up to the DC limit. Additionally, we see similar behavior for various chain lengths ($N_m = 100, 150, 200,$ and 300) where the chain compression for longer chains occurs at lower frequencies. This dependence on chain length is shown in Fig. 9. A scaling of $\nu_c \sim N_m^{-0.75}$ for the critical frequency with chain length is retrieved by superimposing all the curves onto each other.

C. Transient dynamics under DC

In this section, we investigate the initial state dynamics involved in shaping exquisite structures such as the tadpole state and compressed state seen under DC and AC fields. In the previous section, we saw that a chain, specifically under high fields, stabilizes into a tadpole shape with a long extended tail in the DC limit. Interestingly, the dynamic pathway of the formation of this tadpole under DC involves an intermittent stage in which the chain collapses, then is followed by an extension [39,40]. We corroborate this by conducting 50 independent trial runs of the chain under a DC field, where we observe how its structure evolves with time before stabilizing into a tadpole shape. We observed two distinct trajectories of the chain. In most trials, the chain undergoes intermittent
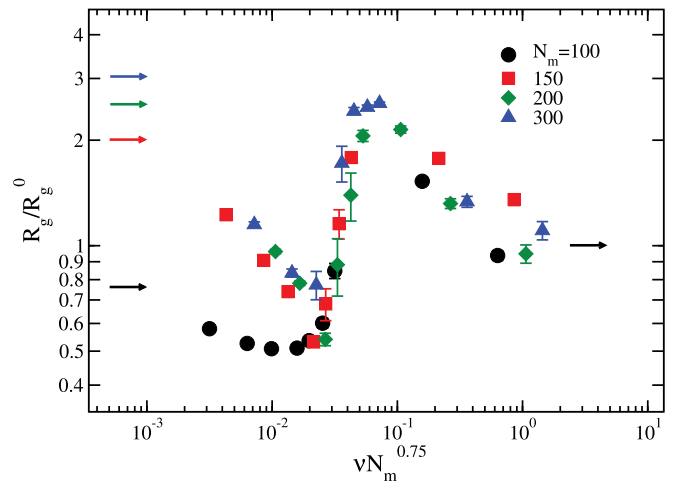
compaction after a weak initial stretching (see Fig. 10, blue curve), further followed by stretching to the tadpole state, while in the rest of the trials, the chain exhibits continual stretching. The trajectories following only stretching initially start with a small headlike structure that grows over time to form an extended tadpole. These distinct pathways are elucidated in Figs. 10(a) and 10(b). The blue curve represents the variation in a maximum extension of the chain X with time, averaged over all those ensembles where the chain undergoes intermittent compression before stretching to a tadpole. Similarly, the red curve pertains to the conformation change with time for all those ensembles where no initial compaction is seen and the chain executes straight stretching.

Consider the case where the chain undergoes an initial compression at a short time, followed by stretching under the DC field. Now, if the field direction is suddenly switched in the opposite direction when the chain acquires the compressed state, the chain may not be able to relax completely and may forbid the stretching to a tadpole that occurs at a later stage under the constant field. Further, if the chain is not given enough time to stretch in all the successive field
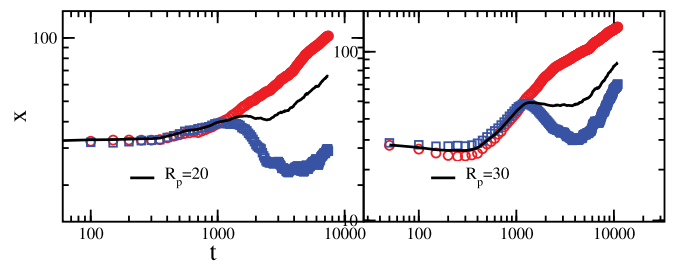
FIG. 10. The average maximum extension of the chain as a function time under a DC field for pore radius $R_p = 20$ (left panel) and $R_p = 30$ (right panel) at $G = 2.0$. The solid line shows the average over all the confirmations. The red line shows the average over trajectories that undergo straight stretching, while the blue is for those which undergo initial compaction followed by stretching.
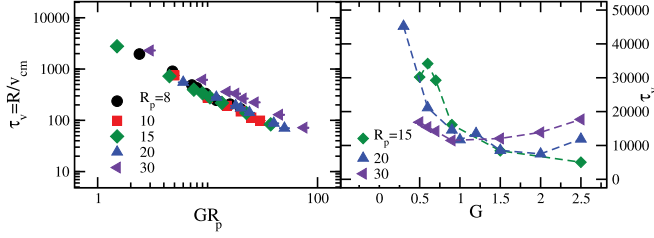
FIG. 11. (a) Recirculation timescale $\tau_v = R_0/v_{cm}$ for different pores as a function of varying field strength G in DC. (b) The DC relaxation timescale is obtained from the correlation of the maximum extension.

switches under AC, the chain might get stuck in this partially stabilized compressed state. Importantly, the timescale of the compressed state obtained under DC in the transient phase falls within the window of $t_c = 1000$–$10\,000$, which coincides with the frequency window of chain collapse seen in AC, i.e., $\nu = 1/t_c = 0.001 - 0.0001$ [see Figs. 6(b) and 6(c)]. Hence, it is safe to assert that for an optimum frequency of field switch, an oscillating field retains the initial compression forbidding extension of the tadpolar structure obtained under DC [see Fig. 4(a)].

Further, we saw in the previous sections that the chain compaction under DC is a result of a recirculating flow field. Under such a scenario, a diffusive timescale of the chain can be given as $\tau_D = \frac{R^3}{\mu_0 a k_B T}$, where the chain traverses a distance of its own size in equilibrium. Similarly, there exists a drift timescale of the chain ($\tau_v = R/v_G$), which essentially signifies the time any part of the chain takes to traverse a distance of R under the field, enforcing proper recirculatory dynamics. The latter is a precursor to obtaining chain compaction under DC. Hence, in the case of an oscillating field at G, if the time period of the applied field follows $1/\nu > \tau_v(G)$ [i.e., $\nu < 1/\tau_v(G)$], the chain is allowed proper recirculating dynamics leading to a compact state in AC. This recirculation timescale as a function of G_{DC} is presented in Fig. 11(a). Since, in our case, τ_v spans a window of $\tau_v = 100$–1000, roughly translating as $1/\tau_v = 0.01$–0.001, then $1/\tau_v$ provides a frequency window below which chain compaction can be obtained. However, at much lower frequencies (i.e., larger allowed times) under the field, the tail extension again becomes prominent, leading to the DC limit. As a result, the compaction is seen only in a narrow window. The above analysis roughly sets the upper-frequency cutoff for the collapse to reinforce. The lower-frequency cutoff for the oscillating field below which the chain reaches to the DC limit can be obtained from the relaxation of the maximum extension under the DC field. The relaxation of the maximum extension is defined as $C_X(t) = \frac{\langle \delta X(t) \delta X(0) \rangle}{\langle \delta X(0) \delta X(0) \rangle}$, where $\delta X = X(t) - \langle X(t) \rangle$ is the fluctuation in maximum extension, and $X(t)$ and $\langle X(t) \rangle$ are the instantaneous and average maximum extension, respectively. The correlation shows exponential decay in a short-time limit, followed by oscillatory behavior for the large-time limit. The behavior of the correlation can be parametrized by the following expression: $C_X(t) = a_0 \exp(-t/\tau) \cos(\frac{2\pi t}{T})$. The retrieved zero crossing time τ_X^{DC} at which $C_X(\tau_X^{DC}) = 0$ is shown in Fig. 11(b) for

varying G with different pore radii. The obtained relaxation time τ_X^{DC} falls in the range of $10\,000$–$40\,000$, which translates to $1/\tau_X^{DC} = 0.0001$–0.000025. This signifies that beyond τ_X^{DC}, the chain attains proper conformational relaxation of its fluctuating head and tail ends. This results in stretched tadpole states seen in the frequency window $\nu \ll \nu_c$ corresponding to the DC limit.

In summary, this section provides an account of the optimum AC frequency range for the chain compression in terms of the recirculation time and initial compaction seen under DC. Further, the cutoff frequencies marking the DC limits for the chain conformations are reasoned in terms of the chain's longest relaxation time, i.e., the relaxation timescale of its maximum extension.

D. Field-induced knotting

Our goal is to corroborate the presence of knots driven by the AC field and how frequency modulation influences knotting tendency and complexity. For this purpose, we use a software package KYMOKNOT [71], which uses the arc closure algorithm for the analysis of knotted structures in linear chains [72,73]. Notably, the average fragment l_h that is part of a knot exhibits a nonmonotonic behavior with frequency for various pore radii, as depicted in Fig. 12(a). The l_h shows the extent of knotted length feasible within a polymer under the field. In the equilibrium or at a higher-frequency limit (such as for $R_p = 20$, $\nu \geqslant 5 \times 10^{-3}$), we found $l_h = 0$, which indicates that the structure is devoid of any such knots, while for the intermediate frequencies, the value of l_h sharply grows, even reaching beyond 0.5, suggesting an enhanced knotting favorability, where a large portion of the chain is topologically entangled. The attainability of the chain self-entanglement to such a vast extent ensues from the oscillatory nature of the inducing field, leading to crumbled structures with low structural expansion. Further, as we go to the DC limit ($\nu \ll 10^{-4}$, l_h is shown with arrows), the fraction constituting the knot falls off dramatically, but exhibits a nonzero l_h [see Fig. 12(a)]. In DC, the formation of a well-taut and stretched tadpole constitutes a tightly knotted head [see Fig. 12(b)(ii)], resulting in smaller values of l_h, contrary to the loosely formed knotted fragments observed at intermediate frequencies in AC [see Fig. 12(b)(i)]. This can be understood by considering a piece of rope with a simple knot tied such that, if we pull the chain from its terminus, the knotted part will become tight and localized. The top row (i) and (ii) of Fig. 12(b) shows the native chain structures formed under the field (the knotted portion is in orange). In contrast, the bottom row (iii) and (iv) shows the corresponding tight and localized knot formed after stretching the field-favored native structures at its extremities.

IV. DISCUSSION

Using a generic bead-spring model, we have presented the phenomenon of chain collapse orchestrated by direct and oscillatory fields. Under the DC field, a polymer chain experiences an inhomogeneous hydrodynamic drag from its interior to the surface, resulting in an overall recirculatory flow field. While flexible chains tend to form extended tadpole structures, a polymer chain with finite bending rigidity beyond a
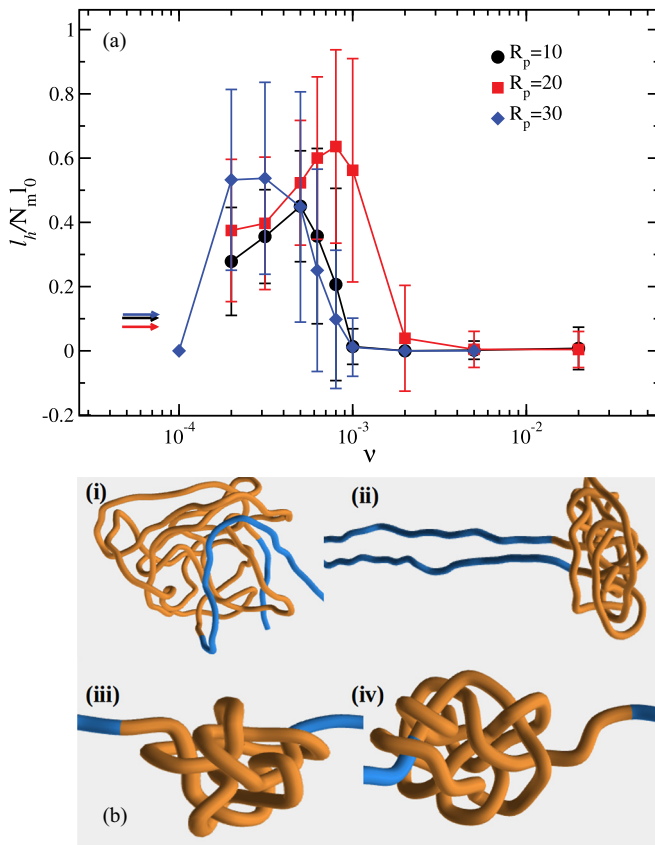
FIG. 12. (a) The fraction of chain length l_h that constitutes a knot as a function ν at field strength $G = 2.0$ under an AC field, for different pore radii obtained using KYMOKNOT software [71]. The error bar depicts the standard deviation at each frequency. (b) The top row depicts a few snapshots of the chain conformations obtained under the field, with the knotted portion highlighted. The bottom row corresponds to the tight and localized knots obtained after stretching respective conformations at its ends.

certain threshold exhibits strong coupling to the force field. This coupling effectuates swirling repetitive segmental motions from the center to the surface of the coil, resulting in intrachain intertwinings and overall chain compression. Also, stronger confinements instigate this compressive effect even for smaller bending rigidities, plausibly due to the enhanced segmental crowding and increased apparent stiffness induced by the tube.

Apart from the confinement and chain rigidity, the nature of the jostling force also brings fascinatingly complex dynamics

into the picture [74–76]. Following this, we elucidate that a semiflexible chain under an oscillating field exhibits remarkable compression in certain frequency windows. The AC field orchestrated compression is attainable across a wide range of confinements (including bulk), bending rigidities, and field strengths, where the chain typically stretches under DC. The field switching under AC captures the initial recirculating flow-induced compaction, forbidding proper tail extension such that the chain essentially gets arrested in a collapsed state with fluctuating ends.

In general, a polyelectrolyte bearing uniform charge on its surface tends to stretch under an electric field because of strong anisotropic polarization along the chain due to counterion cloud shift [13,14,27–33]. However, in a recent work, a counterintuitive shrinkage was reported in a charged flexible polyelectrolyte chain under an AC field, manifested as chain folding [34]. Here, the chain's folding primarily stems from the hydrodynamic interactions, while factors such as charges play a secondary role in the collapse mechanism. Also, the polarization of ions along with other system-relevant length scales and timescales such as the chain's relaxation time exhibits strong coupling with the time period of the applied field. However, it is preestablished that a dsDNA acts as a prototypical wormlike semiflexible chain, where the chain's bending rigidity dominates over large length scales [77]. Our findings further substantiate this, where it captures the collapse dynamics even with a generic semiflexible chain similar to the strong isotropic compression exhibited by DNA under field in experiments [24,26].

Further, this study of conformational changes in macromolecules under strong alternating fields has wider implications in biology. Within the cellular structure, self-organization and dynamical instabilities cause mechanical oscillations [78]. These periodic jostling forces might profoundly influence the conformations of the biopolymer mediated via the cellular fluid. Also, its applicability extends to dielectrophoresis (DEP) experiments [26,79,80] which involves high oscillatory fields employed for more controlled manipulation and efficient separation schemes for DNA and other polymers.

[1] J. Han and H. G. Craighead, Separation of long DNA molecules in a microfabricated entropic trap array, Science **288**, 1026 (2000).

[2] M. Muthukumar, *Polymer Translocation* (Taylor & Francis, USA, 2011).

[3] D. Branton, D. W. Deamer, A. Marziali, H. Bayley, S. A. Benner, T. Butler, M. Di Ventra, S. Garaj, A. Hibbs, X. Huang *et al.*, The potential and challenges of nanopore sequencing, Nat. Biotechnol. **26**, 1146 (2008).

[4] S. Benner, R. J. Chen, N. A. Wilson, R. Abu-Shumays, N. Hurt, K. R. Lieberman, D. W. Deamer, W. B. Dunbar, and M. Akeson, Sequence-specific detection of individual DNA polymerase complexes in real time using a nanopore, Nat. Nanotechnol. **2**, 718 (2007).

[5] P. Chen, J. Gu, E. Brandin, Y.-R. Kim, Q. Wang, and D. Branton, Probing single DNA molecule transport using fabricated nanopores, Nano Lett. **4**, 2293 (2004).

[6] I. Vodyanoy and S. Bezrukov, Sizing of an ion pore by access resistance measurements, Biophys. J. **62**, 10 (1992).

[7] J. J. Kasianowicz, E. Brandin, D. Branton, and D. W. Deamer, Characterization of individual polynucleotide molecules using a membrane channel, Proc. Natl. Acad. Sci. **93**, 13770 (1996).

[8] C. Y. Kong and M. Muthukumar, Modeling of polynucleotide translocation through protein pores and nanotubes, Electrophoresis **23**, 2697 (2002).

[9] B. M. Venkatesan and R. Bashir, Nanopore sensors for nucleic acid analysis, Nat. Nanotechnol. **6**, 615 (2011).

[10] I. M. Derrington, T. Z. Butler, M. D. Collins, E. Manrao, M. Pavlenok, M. Niederweis, and J. H. Gundlach, Nanopore DNA sequencing with MSPA, Proc. Natl. Acad. Sci. **107**, 16060 (2010).

[11] B.-j. Jeon and M. Muthukumar, Polymer capture by α-hemolysin pore upon salt concentration gradient, J. Chem. Phys. **140**, 015101 (2014).

[12] C. T. A. Wong and M. Muthukumar, Polymer translocation through α-hemolysin pore with tunable polymer-pore electrostatic interaction, J. Chem. Phys. **133**, 045101 (2010).

[13] M. Jonsson, U. Jacobsson, M. Takahashi, and B. Nordén, Orientation of large DNA during free solution electrophoresis studied by linear dichroism, J. Chem. Soc., Faraday Trans. **89**, 2791 (1993).

[14] R. Netz, Nonequilibrium Unfolding of Polyelectrolyte Condensates in Electric Fields, Phys. Rev. Lett. **90**, 128104 (2003).

[15] S. P. Singh and M. Muthukumar, Electrophoretic mobilities of counterions and a polymer in cylindrical pores, J. Chem. Phys. **141**, 114901 (2014).

[16] T. Odijk, Scaling theory of DNA confined in nanochannels and nanoslits, Phys. Rev. E **77**, 060901(R) (2008).

[17] A. Muralidhar, D. R. Tree, and K. D. Dorfman, Backfolding of wormlike chains confined in nanochannels, Macromolecules **47**, 8446 (2014).

[18] D. Stein, F. H. J. Heyden, W. J. A. Koopmans, and C. Dekker, Pressure-driven transport of confined DNA polymers in fluidic channels, Proc. Natl. Acad. Sci. USA **103**, 15853 (2006).

[19] R. M. Jendrejack, D. C. Schwartz, J. J. de Pablo, and M. D. Graham, Shear-induced migration in flowing polymer solutions: Simulation of long-chain DNA in microchannels, J. Chem. Phys. **120**, 2513 (2004).

[20] R. M. Jendrejack, E. T. Dimalanta, D. C. Schwartz, M. D. Graham, and J. J. de Pablo, DNA Dynamics in a Microchannel, Phys. Rev. Lett. **91**, 038102 (2003).

[21] R. Chelakkot, R. G. Winkler, and G. Gompper, Migration of semiflexible polymers in microcapillary flow, Europhys. Lett. **91**, 14001 (2010).

[22] D. Steinhauser, S. Köster, and T. Pfohl, Mobility gradient induces cross-streamline migration of semiflexible polymers, ACS Macro Lett. **1**, 541 (2012).

[23] O. A. Hickey and C. Holm, Electrophoretic mobility reversal of polyampholytes induced by strong electric fields or confinement, J. Chem. Phys. **138**, 194905 (2013).

[24] J. Tang, N. Du, and P. S. Doyle, Compression and self-entanglement of single DNA molecules under uniform electric field, Proc. Natl. Acad. Sci. **108**, 16153 (2011).

[25] C. Zhou and R. Riehn, Collapse of DNA under alternating electric fields, Phys. Rev. E **92**, 012714 (2015).

[26] C. Zhou, W. W. Reisner, R. J. Staunton, A. Ashan, R. H. Austin, and R. Riehn, Collapse of DNA in ac Electric Fields, Phys. Rev. Lett. **106**, 248103 (2011).

[27] M. Ueda, H. Oana, Y. Baba, M. Doi, and K. Yoshikawa, Electrophoresis of long DNA molecules in linear polyacrylamide solutions, Biophys. Chem. **71**, 113 (1998).

[28] M. Ueda, Dynamics of long DNA confined by linear polymers, J. Biochem. Biophys. Methods **41**, 153 (1999).

[29] N. Kaji, M. Ueda, and Y. Baba, Stretching of megabase-sized deoxyribonucleic acid molecules by tuning electric-field frequency, Appl. Phys. Lett. **83**, 3413 (2003).

[30] H. Liu, Y. Zhu, and E. Maginn, Molecular simulation of polyelectrolye conformational dynamics under an ac electric field, Macromolecules **43**, 4805 (2010).

[31] P.-Y. Hsiao, Y.-F. Wei, and H.-C. Chang, Unfolding collapsed polyelectrolytes in alternating-current electric fields, Soft Matter **7**, 1207 (2011).

[32] S. Frank and R. G. Winkler, Mesoscale hydrodynamic simulation of short polyelectrolytes in electric fields, J. Chem. Phys. **131**, 234905 (2009).

[33] R. Netz, Polyelectrolytes in electric fields, J. Phys. Chem. B **107**, 8208 (2003).

[34] K. Radhakrishnan and S. P. Singh, Collapse of a confined polyelectrolyte chain under an ac electric field, Macromolecules **54**, 7998 (2021).

[35] M. C. Lagomarsino, I. Pagonabarraga, and C. P. Lowe, Hydrodynamic Induced Deformation and Orientation of a Microscopic Elastic Filament, Phys. Rev. Lett. **94**, 148104 (2005).

[36] X. Schlagberger and R. Netz, Anomalous birefringence and polarizability saturation of charged elastic rods: Field-strength, salt and finite-concentration effects, Europhys. Lett. **83**, 36003 (2008).

[37] S. P. Singh, G. Gompper, and R. G. Winkler, Steady state sedimentation of ultrasoft colloids, J. Chem. Phys. **148**, 084901 (2018).

[38] C. Sendner and R. Netz, Single flexible and semiflexible polymers at high shear: Non-monotonic and non-universal stretching response, Eur. Phys. J. E **30**, 75 (2009).

[39] X. Schlagberger and R. R. Netz, Anomalous Polymer Sedimentation Far from Equilibrium, Phys. Rev. Lett. **98**, 128301 (2007).

[40] X. Schlagberger and R. R. Netz, Anomalous sedimentation of self-avoiding flexible polymers, Macromolecules **41**, 1861 (2008).

[41] V. V. Rybenkov, N. R. Cozzarelli, and A. V. Vologodskii, Probability of DNA knotting and the effective diameter of the DNA double helix, Proc. Natl. Acad. Sci. **90**, 5307 (1993).

[42] X. R. Bao, H. J. Lee, and S. R. Quake, Behavior of Complex Knots in Single DNA Molecules, Phys. Rev. Lett. **91**, 265506 (2003).

[43] R. W. Deibler, S. Rahmati, and E. L. Zechiedrich, Topoisomerase IV, alone, unknots DNA in *e. coli*, Genes Dev. **15**, 748 (2001).

[44] Y. Arai Jr, R. Yasuda, K.-i. Akashi, Y. Harada, H. Miyata, K. Kinosita, and H. Itoh, Tying a molecular knot with optical tweezers, Nature (London) **399**, 446 (1999).

[45] W. R. Taylor and K. Lin, Protein knots: A tangled problem, Nature (London) **421**, 25 (2003).

[46] P. Virnau, L. A. Mirny, and M. Kardar, Intricate knots in proteins: Function and evolution, PLoS Comput. Biol. **2**, e122 (2006).

[47] S. Amin, A. Khorshid, L. Zeng, P. Zimny, and W. Reisner, A nanofluidic knot factory based on compression of single DNA in nanochannels, Nat. Commun. **9**, 1506 (2018).

[48] G. D'Adamo and C. Micheletti, Molecular crowding increases knots abundance in linear polymers, Macromolecules **48**, 6337 (2015).

[49] R. Matthews, A. A. Louis, and C. N. Likos, Effect of bending rigidity on the knotting of a polymer under tension, ACS Macro Lett. **1**, 1352 (2012).

[50] E. Orlandini, M. Tesi, and S. Whittington, Entanglement complexity of semiflexible lattice polygons, J. Phys. A: Math. Gen. **38**, L795 (2005).

[51] H. Zhu, F. Tian, L. Sun, S. Wang, and L. Dai, Revisiting the nonmonotonic dependence of polymer knotting probability on the bending stiffness, Macromolecules **54**, 1623 (2021).

[52] C. H. Nakajima and T. Sakaue, Localization and size distribution of a polymer knot confined in a channel, Soft Matter **9**, 3140 (2013).

[53] C. Micheletti and E. Orlandini, Knotting and metric scaling properties of DNA confined in nanochannels: A Monte Carlo study, Soft Matter **8**, 10959 (2012).

[54] J. G. Reifenberger, K. D. Dorfman, and H. Cao, Topological events in single molecules of *e. coli* DNA confined in nanochannels, Analyst **140**, 4887 (2015).

[55] R. Kapral, Multiparticle collision dynamics: Simulation of complex systems on mesoscales, Adv. Chem. Phys. **140**, 89 (2008).

[56] G. Gompper, T. Ihle, D. M. Kroll, and R. G. Winkler, Multiparticle collision dynamics: A particle-based mesoscale simulation approach to the hydrodynamics of complex fluids, Adv. Polym. Sci. **221**, 1 (2009).

[57] M. Ripoll, K. Mussawisade, R. G. Winkler, and G. Gompper, Low-Reynolds-number hydrodynamics of complex fluids by multi-particle-collision dynamics, Europhys. Lett. **68**, 106 (2004).

[58] A. Malevanets and R. Kapral, Mesoscopic model for solvent dynamics, J. Chem. Phys. **110**, 8605 (1999).

[59] A. Lamura, G. Gompper, T. Ihle, and D. Kroll, Multi-particle collision dynamics: Flow around a circular and a square cylinder, Europhys. Lett. **56**, 319 (2001).

[60] I. Ali, D. Marenduzzo, and J. M. Yeomans, Polymer Packaging and Ejection in Viral Capsids: Shape Matters, Phys. Rev. Lett. **96**, 208102 (2006).

[61] C. R. Locker and S. C. Harvey, A model for viral genome packing, Multiscale Model. Simulat. **5**, 1264 (2006).

[62] P. J. Hagerman, Flexibility of DNA, Annu. Rev. Biophys. Biophys. Chem. **17**, 265 (1988).

[63] M. Daoud and P. De Gennes, Statistics of macromolecular solutions trapped in small pores, J. Phys. France **38**, 85 (1977).

[64] Y. Wang, D. R. Tree, and K. D. Dorfman, Simulation of DNA extension in nanochannels, Macromolecules **44**, 6594 (2011).

[65] W. Reisner, J. N. Pedersen, and R. H. Austin, DNA confinement in nanochannels: Physics and biological applications, Rep. Prog. Phys. **75**, 106601 (2012).

[66] T. Odijk, The statistics and dynamics of confined or entangled stiff polymers, Macromolecules **16**, 1340 (1983).

[67] L. Coronel, E. Orlandini, and C. Micheletti, Nonmonotonic knotting probability and knot length of semiflexible rings: The competing roles of entropy and bending energy, Soft Matter **13**, 4260 (2017).

[68] P. Poier, C. N. Likos, and R. Matthews, Influence of rigidity and knot complexity on the knotting of confined polymers, Macromolecules **47**, 3394 (2014).

[69] Z. Benková and P. Cifra, Simulation of semiflexible cyclic and linear chains moderately and strongly confined in nanochannels, Macromolecules **45**, 2597 (2012).

[70] See Supplemental Material at http://link.aps.org/supplemental/10.1103/PhysRevE.108.014501 for compression of a confined semiflexible polymer under direct and oscillating fields.

[71] L. Tubiana, G. Polles, E. Orlandini, and C. Micheletti, Kymoknot: A web server and software package to identify and locate knots in trajectories of linear or circular polymers, Eur. Phys. J. E **41**, 72 (2018).

[72] L. Tubiana, E. Orlandini, and C. Micheletti, Multiscale Entanglement in Ring Polymers under Spherical Confinement, Phys. Rev. Lett. **107**, 188302 (2011).

[73] L. Tubiana, E. Orlandini, and C. Micheletti, Probing the entanglement and locating knots in ring polymers: A comparative study of different arc closure schemes, Prog. Theor. Phys. Suppl. **191**, 192 (2011).

[74] A. Belmonte, M. J. Shelley, S. T. Eldakar, and C. H. Wiggins, Dynamic Patterns and Self-Knotting of a Driven Hanging Chain, Phys. Rev. Lett. **87**, 114301 (2001).

[75] B. W. Soh, I. R. Gengaro, A. R. Klotz, and P. S. Doyle, Self-entanglement of a tumbled circular chain, Phys. Rev. Res. **1**, 033194 (2019).

[76] E. Ben-Naim, Z. A. Daya, P. Vorobieff, and R. E. Ecke, Knots and Random Walks in Vibrated Granular Chains, Phys. Rev. Lett. **86**, 1414 (2001).

[77] C. Bustamante, J. Marko, E. Siggia, and S. Smith, Entropic elasticity of λ-phage DNA, Science **265**, 1599 (1994).

[78] K. Kruse and F. Jülicher, Oscillations in cell biology, Curr. Opin. Cell Biol. **17**, 20 (2005).

[79] M. Viefhues and R. Eichhorn, DNA dielectrophoresis: Theory and applications a review, Electrophoresis **38**, 1483 (2017).

[80] C. L. Asbury, A. H. Diercks, and G. Van Den Engh, Trapping of DNA by dielectrophoresis, Electrophoresis **23**, 2658 (2002).